Available online at www.sciencedirect.com
SCIENCE DIRECT®
Journal of Magnetic Resonance 158 (2002) 126–142
JMR Journal of Magnetic Resonance
www.academicpress.com

Characteristics of ESEEM and HYSCORE spectra of $S > 1/2$ centers in orientationally disordered systems

Nikolas Ploutarch Benetis, Paresh C. Dave, and Daniella Goldfarb*

Department of Chemical Physics, Weizmann Institute of Science, Rehovot 76100, Israel

Received 15 April 2002; revised 17 July 2002

Abstract

One- and two-dimensional electron-spin echo envelope modulation (ESEEM) spectra of Kramers' multiplets in orientationally disordered systems are simulated using a simple mathematical model. A fairly general high-field spin Hamiltonian is considered with a general **g**-tensor and arbitrary relative orientations between all tensors involving the electron-spin S, the nuclear spin I, and their interaction. The zero field splitting (ZFS) and the nuclear quadrupole interactions are, however, approximated by their respective secular part in a way that retains all orientation dependencies and it is assumed that the nuclear quadrupole interaction is smaller than the hyperfine interaction. These approximations yield an effective sublevel nuclear Hamiltonian for each EPR transition and are sufficient to account for the most important characteristics of the ESEEM spectra of high electronic multiplets in orientationally disordered systems. Moreover, they allow to obtain some analytical expressions that for $I = 1/2$ illuminate important aspects of 2D hyperfine sublevel correlation (HYSCORE) experiments in $S = 3/2$, 5/2 systems. The pulses are considered as ideal and selective with respect to the different EPR transitions. The contributions of the latter to the echo intensity are weighed according to their different nutation angles and equilibrium Boltzmann populations. For simple axial cases with $I = 1/2$, analytical expressions, analogous to the $S = 1/2$ case, were derived for: (i) the modulation depth, (ii) the lineshapes of the HYSCORE cross-correlation ridges, and (iii) ENDOR powder pattern. Experimental results obtained from $Mn(D_2O)_6^{2+}$ and $VO(D_2O)_5^{2+}$ in frozen solutions are presented, compared, and analyzed in light of the theoretical part.

1. Introduction

Electron–spin echo envelope modulation (ESEEM) spectroscopy has become a well-established technique for the investigation of transition metal centers in a large variety of systems and disciplines ranging from physics to chemistry and biology. In recent years, the number of available ESEEM pulse sequences has increased significantly and it includes a variety of one-dimensional (1D) and two-dimensional (2D) experiments [1–3]. One of the most useful ESEEM experiment is the 2D hyperfine sublevel correlation (HYSCORE) experiment, which correlates nuclear transition frequencies belonging to different electron-spin, M_S, manifolds [4]. Most of the ESEEM applications have so far been carried out on $S = 1/2$ systems. In this case, the theory is well established and the characteristics of the spectra obtained from the different pulse sequences are well understood [5–7]. General expressions for the echo intensity generated by the various experiments have been derived, thus, allowing to perform spectral simulations, which are necessary for the interpretation of the spectra and the extraction of the spin Hamiltonian parameters [5,6,8]. In general, the majority of the theoretical derivations follow the pioneering work of Mims [9] where the density matrix formalism is used, ideal pulses are assumed, and the spin Hamiltonian is expressed in a block diagonal form. Each block in the Hamiltonian matrix represents an effective nuclear Hamiltonian accounting for the nuclear manifolds within the two electron-spin states, α and β.

There are many systems of interest, which involve metal ions with $S > 1/2$ which, in principle, should be amenable to ESEEM investigations. The case of non-Kramers' ions with a dominating zero field splitting (ZFS) interaction was worked out for $S = 2$ by Hoffman and coworkers [10]. A few examples of ESEEM applications for half integer $S > 1/2$ spin systems have been

* Corresponding author. Fax: +972-8-9344123.
E-mail address: daniella.goldfarb@weizmann.ac.il (D. Goldfarb).

1090-7807/02/$ - see front matter © 2002 Elsevier Science (USA). All rights reserved.
PII: S1090-7807(02)00066-6

reported so far and most of them have been analyzed either qualitatively or by assuming an effective $S = 1/2$ system [11–13]. These include transition metals such as Mn(II) and Fe(III), which are important ions in Chemistry and Biology. Therefore, the ESEEM theory should be extended to include high-spin systems, to allow extensive data analysis, followed by a critical evaluation of the effectiveness and limitations of the method.

The notion that $S = 5/2$ systems behave differently than those with $S = 1/2$ was already noted by Mims et al. [14] who suggested to treat it as a superposition of independent effective $S = 1/2$ Hamiltonians. The first theoretical attempt to deal with two- and three-pulse ESEEM for $S = 5/2$ systems was carried out by Coffino and Peisach [15]. They introduced important aspects such as the inclusion of microwave (MW) irradiation in the simulations, showing the EPR transition selectivity in the presence of an appreciable ZFS with a dominating electron Zeeman interaction. They also showed that the contribution of all EPR transitions should be considered, since the modulation frequencies of the various transitions are different. Moreover, they took into account non-secular terms of the ZFS Hamiltonian and using numerical diagonalization they found out that the time domain ESEEM traces were affected by the ZFS in a way that does not change significantly the nuclear modulation frequencies. Furthermore, the authors considered simultaneously both the hyperfine interaction (hfi) of the ^{55}Mn nucleus and of a ligand nucleus. They reported that the ^{55}Mn coupling does not affect the ESEEM frequencies of the ligand. A more qualitative and pictorial representation of the two- and three-pulse ESEEM has been reported by Larsen et al. [16]. There, the $S = 1/2, 5/2$ cases are visualized in a graphic form, revealing the variation of the effective fields "seen" by the nucleus in the different sublevels due to variation of the hfi.

In the present work, we extend Mims' theory [9], aiming towards reasonably accurate and simultaneously quick simulations of both 1D ESEEM (up to four pulses) and 2D HYSCORE experiments in orientationally disordered systems. The HYSCORE characteristics for $S = 5/2$ have not been examined so far. A particularly important issue is whether correlations observed from the various EPR transitions can have a significant effect on the complexity of the spectrum as compared to the $S = 1/2$ case. The present derivations are applicable to higher Kramers' multiplets coupled to an arbitrary nuclear spin, but include only the *S*- and *I*-secular terms in the ZFS and the nuclear quadrupole interactions (nqi), respectively. According to Coffino et al. [15] and Vardi et al. [17], the non-secular ZFS terms of the Hamiltonian do not affect the nuclear ENDOR/ESEEM frequencies for relatively small hyperfine couplings and therefore they have been neglected in the present work.

In the following, we first present the spin Hamiltonian used, its block diagonal representation, and with that the definition of the effective nuclear sublevel Hamiltonians, one for each electron-spin state. We give expressions for the eigenvalues and eigenvectors of the sublevel Hamiltonians, which are then incorporated into the generalized echo expressions for two-, three-, and four-pulse ESEEM and 2D HYSCORE experiments (Fig. 1a). This is followed by a discussion of the different nutation frequencies of the various EPR transitions and their effect on the relative contributions of these EPR transitions to the total echo intensity. A series of spectral simulations is presented, illustrating the characteristics of the 2D HYSCORE spectra expected under various conditions and the properties of the sum combination peak in two- and four-pulse experiments. The appendices present analytical expressions for $I = 1/2$ case for the modulation depth and cross-peak lineshapes. Finally, some experimental HYSCORE spectra of $Mn(D_2O)_6^{2+}(S = 5/2)$ are compared to those of $VO(D_2O)_5^{2+}(S = 1/2)$ and analyzed in terms of the presented theoretical analysis.

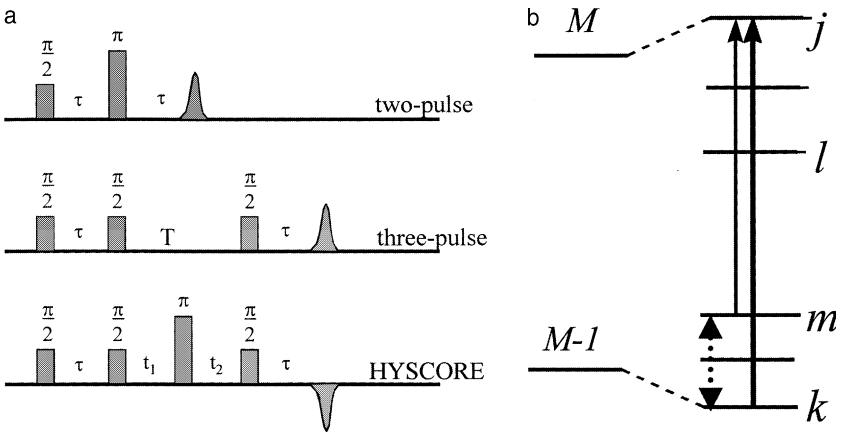

Fig. 1. (a) The pulse sequences of the two- and three-pulse ESEEM and HYSCORE experiments. (b) A schematic representation of the energy-level diagram showing the interrelation of the $(M \leftrightarrow M-1)$ allowed EPR transition $(m \leftrightarrow j)$, the forbidden EPR transition $(k \leftrightarrow j)$ and the corresponding ESEEM frequency $(m \leftrightarrow k)$, shown by a dotted arrow. The labels of the nuclear states *j*, *k*, *l*, *m* are the unmixed nuclear projections.

2. Theory

2.1. The spin Hamiltonian, eigenvalues, and eigenvectors within the automatic diagonalization limit

The spin Hamiltonian for an $S > 1/2$ system interacting with a nucleus with a spin I is:

$$H = \beta \mathbf{B}\cdot\mathbf{g}\cdot\hat{\mathbf{S}} + \hat{\mathbf{S}}\cdot\mathbf{D}\cdot\hat{\mathbf{S}} + \hat{\mathbf{S}}\cdot\mathbf{A}\cdot\hat{\mathbf{I}} - g_N\beta_N\mathbf{B}\cdot\hat{\mathbf{I}} + \hat{\mathbf{I}}\cdot\mathbf{Q}\cdot\hat{\mathbf{I}}. \tag{1}$$

The hfi of a paramagnetic metal ion with its own nucleus is not included in the above expression, as it does not affect the ESEEM spectrum [15]. To follow Mims' treatment for $S = 1/2$ [9], the Hamiltonian in Eq. (1) should be partitioned into blocks, each representing a nuclear sublevel Hamiltonian, H_M, tagged by the electron-spin projection M ($\equiv M_S$). This creates $2S + 1$ such Hamiltonians that will be considered as not interacting with each other [15]. The block partitioning can be accomplished under the following circumstances: (i) Small g-anisotropy that can be ignored in the MW irradiation terms (see below) and (ii) the ZFS term is smaller than the electron Zeeman term, and the tensor representing the ZFS, **D**, can be considered only to first order. Moreover, all the interactions are assumed to be S-secular, in accordance with the high-field case. In this work, we use the eigenbasis $\{|SM\rangle|In_M\rangle \forall (-S \leqslant M \leqslant S \text{ and } -I \leqslant n \leqslant I)\}$ obtained from the individually diagonalized H_M's of the direct product S-I-spin space by using the transformations $\mathbf{t}_M$ (see below) [18]. The corresponding sublevel nuclear eigenstates, $|In_M\rangle$, were explicitly written in terms of the regular nuclear basis $\{|In\rangle\}$ for $M = \pm 1/2$ in Ref. [18] and they will be referred here with respect to the M electron-spin state. The explicit form of the eigenbasis is used only to obtain Eqs. (8) and (9) in this work.

The individually diagonalized H_M's are finally given as:

$$H_M^I = \omega_S'(M) + \omega_{I;M} I_z''(M) + \omega_{\mathrm{nqi}}^{(M)} I_z''^2(M). \tag{2}$$

The nuclear spin I has been used as a superscript, indicating a reduced nuclear Hamiltonian H_M with dimensionality $(2I + 1)$. In Eq. (2), $\omega_S'(M)$ corresponds to the exact electron Zeeman frequency with respect to **g** and includes also a first-order correction due the ZFS according to:

$$\omega_S'(M) = M\omega_{0S}' + M^2\omega_{\mathrm{ZFS}}' \quad \text{with } \omega_{0S}' = g'\beta B_0/\hbar, \tag{3}$$

where g' is the effective g-factor [19,20].

The first-order ZFS frequency ω_{ZFS}' is [19]:

$$\omega_{\mathrm{ZFS}}' = \frac{3\mathbf{b}^+\cdot\mathbf{g}\cdot\mathbf{D}\cdot\mathbf{g}^+\cdot\mathbf{b}}{2g'^2}, \tag{4}$$

where **b** is a unit vector along the magnetic field. The so-called electron nuclear double resonance (ENDOR) frequencies, $\omega_{I;M}$, are first given in a vectorial form $\underline{\omega}_{I;M}$ in angular frequency units [19,20]:

$$\underline{\omega}_{I;M} = \mathbf{G}_M\mathbf{b} \quad \text{with } \mathbf{G}_M = (M/g')\mathbf{g}\mathbf{A} + \omega_{0I}\mathbf{1}, \tag{5}$$

where $\omega_{0I} = -g_N\beta_N B_0/\hbar$ is the nuclear Larmor frequency. The magnitude, $\omega_{I;M} = |\underline{\omega}_{I;M}| = (\mathbf{b}^+\mathbf{G}_M^+\mathbf{G}_M\mathbf{b})^{1/2}$ of the nuclear frequency vectors for each electronic sublevel M, was used in Eq. (2). The nqi is also considered here as a first order correction, taking into account only secular terms according to:

$$\omega_{\mathrm{nqi}}^{(M)} = \frac{3\mathbf{b}^+\cdot\mathbf{G}_M^+\cdot\mathbf{Q}\cdot\mathbf{G}_M\cdot\mathbf{b}}{2\omega_{I;M}^2}. \tag{6}$$

To obtain relations (4) and (6), the components of **D** and **Q** were written in the **g** principal frame and rotated to the quantization frame of reference of the electron-spin and the nucleus, respectively, where only terms proportional to S_z' and $I_z''(M)$ were selectively retained. According to the present treatment, the corrections to the modulation frequencies due to the nqi can be added at the last stage of the signal computations by using Eq. (2) for the diagonalized sublevel Hamiltonian, as described in Ref. [18].

Neglecting electron-spin mixing, the EPR transition probabilities that determine the amplitudes of the ESEEM modulations are [21]

$$\begin{aligned} I_{M;n\leftrightarrow M';n'}^{\mathrm{EPR}} &\propto \Delta\rho_{M;M'}|\langle SM|\langle In_M|S_+|SM'\rangle|In_{M'}'\rangle|^2 \\ &= \Delta\rho_{M;M'}\cdot\delta_{M',M-1}\cdot[S(S+1) \\ &\quad - M'(M'+1)]\cdot|\langle In_M|In_{M'}'\rangle|^2 \\ &\equiv \Delta\rho_{M;M'}\cdot\delta_{M',M-1}\cdot C_{M;M'}\cdot|\langle In_M|In_{M'}'\rangle|^2, \end{aligned} \tag{7}$$

where $\Delta\rho_{M;M'}$ is the population difference of the M and M' states, which according to the Boltzmann statistics is given by $\Delta\rho_{M;M'} \equiv \rho_M - \rho_{M'} \propto \exp(-E_M/kT) - \exp(-E_{M'}/kT)$. The mixing of the $|In_M\rangle$ nuclear states of the sublevel Hamiltonian, H_M^I, depends on the M value of corresponding sublevel.

In the $S = 1/2$ case, $M = 1/2$, $M' = -1/2$, and the mutual projection $\langle In_M|In_{M'}'\rangle$ is usually given by the matrix elements of the Mims matrix **M** [9], here denoted as $\mathbf{t}^{M;M'}$ [18]. The latter is the matrix product of the diagonalizing transformations of the two sublevels, i.e., $\mathbf{t}_M^+\mathbf{t}_{M'} \equiv \mathbf{t}^{M;M'}$. This matrix, under autodiagonalization conditions (ideal pulses and consideration of the nqi only to first order), was shown to be proportional to a single matrix element of the Wigner rotation matrix according to [18]:

$$t_{nn'} \equiv \langle In_\alpha|In_\beta'\rangle = d_{nn'}^{(I)}(\vartheta_t), \tag{8}$$

where ϑ_t is the angle between the nuclear quantization axes in the $M = -1/2$ and $M = 1/2$ manifolds.

If the electronic mixing by the ZFS in higher multiplets ($S > 1/2$) can be disregarded, under conditions of selective excitation [14,15] each EPR transition, $M \leftrightarrow M'$, can be considered as an isolated two-level spin system, defined by the projections M, M' [16]. Accordingly, the relations

for $S = 1/2$ can be generalized such that ϑ_t depends on the projections of the electronic transition $M \leftrightarrow M'$ (usually $M' = M - 1$)

$$t_{nn'}^{M;M'} \equiv \langle In_M | In'_{M'} \rangle = d_{nn'}^{(I)}(\vartheta_t^{M;M'}). \tag{9}$$

The $\vartheta_t^{M,M'}$ angles are obtained from the ENDOR frequency vectors, $\underline{\omega}_{I;M}$, according to [16,18]:

$$\underline{\omega}_{I;M} \cdot \underline{\omega}_{I;M'} = |\underline{\omega}_{I;M}||\underline{\omega}_{I;M'}| \cos \vartheta_t^{M;M'}. \tag{10}$$

The final result for the intensity of the electronic transitions is thus simply,

$$I_{M;n\leftrightarrow M';n'}^{\mathrm{EPR}} \propto \Delta\rho_{M;M'} \cdot \delta_{M',M-1} \cdot C_{M;M'} \cdot [d_{nn'}^{(I)}(\vartheta_t^{M;M'})]^2. \tag{11}$$

This approximate relation presents the important factors that should be incorporated for the selective irradiation in the ESEEM simulations.

2.2. Expressions and properties of the echo signals

Considering only the $|\Delta M| = 1$ transitions, the electron-spin echo signal becomes:

$$\mu_x = g\beta \,\mathrm{Re}\left[\sum_{M=-S+1}^{S} \langle S_+ \rangle_{\mathrm{Sequence}}^{M;M-1}\right] \tag{12}$$

and the two-, three-, and four-pulse echo sequences can be obtained using the density matrix formalism according to Mims [9], evolving from the Boltzmann equilibrium by predefined sequences of precession and nutation periods.

The contribution of the transition $M \leftrightarrow M - 1$ to the primary echo is:

$$\begin{aligned}\langle S_+(\tau)\rangle_{2p}^{M;M-1} &= K_{2p}^{M;M-1} \sum_{j,k,l,m} (-1)^{j-k+l-m} d_{jk}^{(I)}(\vartheta_t^{M;M-1}) \\ &\times d_{kl}^{(I)}(\vartheta_t^{M;M-1}) d_{lm}^{(I)}(\vartheta_t^{M;M-1}) d_{mj}^{(I)}(\vartheta_t^{M;M-1}) \\ &\times \exp[-\mathrm{i}(\omega_{I;M-1}^{km} + \omega_{I;M}^{lj})\tau]\end{aligned} \tag{13}$$

and

$$\begin{aligned}K_{2p}^{M;M-1} &= (1/2)\Delta\rho_{M;M-1} C_{M;M-1} \sin \beta_{p1}^{M;M-1} \\ &\times \sin^2(\beta_{p2}^{M;M-1}/2).\end{aligned} \tag{14}$$

In this representation, each EPR transition is treated quantitatively as an effective $S = 1/2$ system with well-defined contributions to the echo that depends on M and $M - 1$. The indices k, m correspond to the nuclear sublevel in the $M - 1$ manifold whereas the l, j indices describe the nuclear sublevels within the M manifold (see Fig. 1b). The modulation frequencies for the nuclear levels i, j are generally defined as the appropriate differences $\omega_{I;M}^{ij} = (E_{I;M}^i - E_{I;M}^j)/\hbar$ of the i and j eigenvalues of the sublevel Hamiltonian H_M^I. They can be computed with any degree of accuracy depending on the method [19,22] and in the limits of the autodiagonalization case [18] they are given by the simple relation $\omega_{I;M}^{ij} = (i - j)\omega_{I;M} + (i^2 - j^2)\omega_{\mathrm{nqi}}^{(M)}$, according to Eq. (2). Practically, only those nuclear frequencies for which $\omega_{1S} = 2\pi g\beta B_1/\hbar > |\omega_{I;M}^{ij}|$, where B_1 is the applied microwave field, will be observed [23]. The angles $\beta_{p1}^{M;M-1}$ and $\beta_{p2}^{M;M-1}$ refer to the nutation angles of the first and second MW pulses, respectively. A maximum echo intensity, determined by $K_{2p}^{M;M-1}$ (Eq. (14)), is obtained for $\beta_{p1}^{M;M-1} = \pi/2$ and $\beta_{p2}^{M;M-1} = \pi$. An analytical expression for the modulation depth for the simple case of $I = 1/2$, derived from the sum of the various $d_{jk}^{(I)}(\vartheta_t^{M;M-1})$ terms, is presented in Appendix A. For the general case (not under autodiagonalization conditions), the expressions developed by Mims for $S = 1/2$ should be used, replacing the $\mathbf{M}$ matrix elements with the appropriate $M_{ij}^{M;M-1}$ matrix elements [9].

The stimulated echo signal (three-pulse ESEEM) from the EPR transition $M \leftrightarrow M - 1$ is given by:

$$\begin{aligned}\langle S_+(\tau;T)\rangle_{3p}^{M;M-1} &\equiv V_M^I(\tau;T) + V_{M-1}^I(\tau;T) \\ &= K_{3p}^{M;M-1} \sum_{j,k,l,m} (-1)^{j-k+l-m} d_{jk}^{(I)}(\vartheta_t^{M;M-1}) d_{kl}^{(I)} \\ &\times (\vartheta_t^{M;M-1}) d_{lm}^{(I)}(\vartheta_t^{M;M-1}) d_{mj}^{(I)}(\vartheta_t^{M;M-1}) \\ &\times \Big\{ \exp[-\mathrm{i}(\omega_{I;M}^{lj} + \omega_{I;M-1}^{km})\tau] \\ &\times \exp(-\mathrm{i}\omega_{I;M}^{lj} T) + \exp[-\mathrm{i}(\omega_{I;M-1}^{lj} \\ &+ \omega_{I;M}^{km})\tau] \exp(-\mathrm{i}\omega_{I;M-1}^{lj} T) \Big\}\end{aligned} \tag{15}$$

with

$$\begin{aligned}K_{3p}^{M;M-1} &= (-1/2)^3 \Delta\rho_{M;M-1} C_{M;M-1} \sin \beta_{p1}^{M;M-1} \\ &\times \sin \beta_{p2}^{M;M-1} \sin \beta_{p3}^{M;M-1}.\end{aligned} \tag{16}$$

In this case, the maximum stimulated echo intensity is obtained for nominal pulse angles of $\pi/2$ for all three pulses.

The expression for the echo intensity in the HYSCORE experiment that contribute to the cross peaks is:

$$\langle S_+(\tau;t_1,t_2)\rangle_{\mathrm{hysc},x}^{M;M-1} \equiv V_{M;M-1,x}^I(\tau;t_1,t_2) + V_{M-1;M,x}^I(\tau;t_1,t_2) \tag{17}$$

and

$$\begin{aligned}V_{M;M-1,\times}^I(\tau;t_1,t_2) &= K_{\mathrm{HYSC};\times}^{M;M-1} \sum_{j,k,l,m,n,p} (-1)^{j-k+l-m+n-p} d_{jk}^{(I)} \\ &\times (\vartheta_t^{M;M-1}) d_{kl}^{(I)}(\vartheta_t^{M;M-1}) d_{lm}^{(I)}(\vartheta_t^{M;M-1}) \\ &\times d_{mn}^{(I)}(\vartheta_t^{M;M-1}) d_{np}^{(I)}(\vartheta_t^{M;M-1}) d_{pj}^{(I)}(\vartheta_t^{M;M-1}) \\ &\times \exp[-\mathrm{i}(\omega_{I;M}^{lj} + \omega_{I;M-1}^{km})\tau] \\ &\times \exp(-\mathrm{i}\omega_{I;M}^{ln} t_1) \exp(-\mathrm{i}\omega_{I;M-1}^{kp} t_2).\end{aligned} \tag{18}$$

The overall intensity coefficients of the cross-correlation peaks are,

$$\begin{aligned}K_{\mathrm{HYSC};\times}^{M;M-1} &= (1/2)^3 \Delta\rho_{M;M-1} C_{M;M-1} \sin \beta_{p1}^{M;M-1} \\ &\times \sin \beta_{p2}^{M;M-1} \sin^2(\beta_{p3}^{M;M-1}/2) \sin \beta_{p4}^{M;M-1}.\end{aligned} \tag{19}$$

In this case, the echo intensity is maximized for nominal angles of $\pi/2$ for p_1, p_2, and p_4, and π for p_3. The echo expression for the 1D four-pulse ESEEM sequence can be derived from Eq. (18) by setting $t_1 = t_2 = t$. Using the properties of the reduced Winger matrix $\mathbf{d}^{(I)}$, it can be shown that in the above expressions the intensity of the echo signals are real quantities [18].

2.3. Nutation frequencies and selective excitation

The nominal pulse angles of the selected EPR transitions are $(M, M-1)$-dependent according to: $\beta_p^{M;M-1} = C_{M;M-1}\omega_{1S}t_p$, where t_p is the pulse duration and $C_{M;M-1}$ is defined in Eq. (7). Consequently, it is impossible to simultaneously maximize the contributions of all EPR transitions to the echo. For the same MW power and pulse duration, the effective nutation angle of the various EPR transitions can be related to that of a reference transition according to:

$$\beta_p^{M;M-1} = \frac{C_{M;M-1}}{C^{S_{\mathrm{ref}}}_{M_{\mathrm{ref}};M_{\mathrm{ref}}-1}}\beta_p^{\mathrm{ref}}. \tag{20}$$

Table 1 lists the effective nutation angles of the various EPR transitions with respect to an $S = 1/2$ system and to the $|-1/2\rangle \leftrightarrow |1/2\rangle$ transition of the $S = 5/2$ sextet. The different nutation frequencies of the various transitions make the relative contribution of each transition to the total echo intensity power dependent. Fig. 2 shows the ω_{1S} dependence of the contribution of the various EPR transitions in a HYSCORE experiment to the echo intensity for pulse durations $t_{p1} = t_{p2} = t_{p4} = 20$ ns and $t_{p3} = 40$ ns, which are typically employed experimentally. In this calculation, only the EPR transition probabilities and the nutation frequencies were taken into account, based on Eq. (19) without considering the different inhomogeneous broadening of the transitions and the temperature. By setting $\omega_{1S}/2\pi = 7.5$ MHz, it should be, in principle, possible to isolate the contributions of the $|\pm 5/2\rangle \leftrightarrow |\pm 3/2\rangle$ transitions. In contrast, the $|\pm 3/2\rangle \leftrightarrow |\pm 1/2\rangle$ and $|-1/2\rangle \leftrightarrow |1/2\rangle$ transitions have very similar nutation profiles and cannot be effectively distinguished by MW power variation.

The different nutation frequencies of the EPR transitions result in significant presence of diagonal peaks in the HYSCORE spectrum as a consequence of incomplete inversion by the third pulse for some of the transitions. The relative intensities of diagonal peaks can be obtain from Eq. (17) with:

$$\begin{aligned} V^I_{M;M-1,a}(\tau;t_1,t_2) = K^{M;M-1}_{\mathrm{HYSC};a} \sum_{j,k,l,m} (-1)^{j-k+l-m} d^{(I)}_{jk}(\vartheta_t^{M;M-1}) \\ \times d^{(I)}_{kl}(\vartheta_t^{M;M-1}) d^{(I)}_{lm}(\vartheta_t^{M;M-1}) d^{(I)}_{mj}(\vartheta_t^{M;M-1}) \\ \times \exp\left[-\mathrm{i}(\omega^{lj}_{I;M} + \omega^{km}_{I;M-1})\tau\right] \\ \times \exp\left[-\mathrm{i}\omega^{lj}_{I;M}(t_1+t_2)\right], \end{aligned} \tag{21}$$

where

$$\begin{aligned} K^{M;M-1}_{\mathrm{HYSC};a} = (1/2)^3 \Delta\rho_{M;M-1} C_{M;M-1} \sin\beta_{p1}^{M;M-1} \\ \times \sin\beta_{p2}^{M;M-1} \cos^2(\beta_{p3}^{M;M-1}/2) \sin\beta_{p4}^{M;M-1}. \end{aligned} \tag{22}$$

In the following, these peaks will be referred to as autocorrelation peaks. Their presence is troublesome as they can mask cross-peaks originating from small hyperfine couplings that are close to the diagonal.

The reason for the non-negligible contribution of the autocorrelation terms here is twofold: (i) The deviations of the nutation angle $\beta_{p3}^{M;M-1}$ from π different for the various transitions and (ii) even though the $\cos^2(\beta_{p3}^{M;M-1}/2)$ factor is small in comparison to $\sin^2(\beta_{p3}^{M;M-1}/2)$ in the cross-correlation term in Eq. (19), it is compensated by the greater amplitudes of the coefficients in the terms of the sums in Eqs. (18) and (21). Because the quantities d_{jk} are typically smaller than a unity, being products of the trigonometric functions of the same transformation angle $\vartheta_t^{M;M-1}$, a four-factor product of the d_{jk} elements in the autocorrelation signal is larger than the six-factor product in the cross-correlation signal.

There are two more factors that have to be taken into account when the relative contributions of the various EPR transitions to the ESEEM/HYSCORE spectra are considered, one is the Boltzmann population and the other is the different inhomogeneous broadening of the EPR transitions in the case of orientationally disordered systems. The contribution of the $|-1/2\rangle \leftrightarrow |1/2\rangle$ transition is the largest, as long as it is within the irradiation bandwidth, because its broadening is only a second order effect [24]. To take explicitly these effects into

Table 1
The effective nutation angles of the various EPR transitions for a $S = 5/2$ system relative to a $S = 1/2$ system and relative to the $|-1/2\rangle \leftrightarrow |1/2\rangle$ transition of a $S = 5/2$ system (see Eq. (20))

Spin S	Reference transition		EPR transition					
	$\lvert-1/2\rangle \leftrightarrow \lvert1/2\rangle$		$\lvert-1/2\rangle \leftrightarrow \lvert1/2\rangle$		$\lvert\pm5/2\rangle \leftrightarrow \lvert\pm3/2\rangle$		$\lvert\pm3/2\rangle \leftrightarrow \lvert\pm1/2\rangle$	
	$\beta_{p1}^{M;M-1}$	$\beta_{p2}^{M;M-1}$	$\beta_{p1}^{M;M-1}$	$\beta_{p2}^{M;M-1}$	$\beta_{p1}^{M;M-1}$	$\beta_{p2}^{M;M-1}$	$\beta_{p1}^{M;M-1}$	$\beta_{p2}^{M;M-1}$
1/2	$\pi/2$	π	$3\pi/2$	3π	$5^{1/2}\pi/2$	$5^{1/2}\pi$	$8^{1/2}\pi/2$	$8^{1/2}\pi$
5/2	$\pi/2$	π	$\pi/2$	π	$(5^{1/2}/6)\pi$	$(5^{1/2}/3)\pi$	$(8^{1/2}/6)\pi$	$(8^{1/2}/3)\pi$

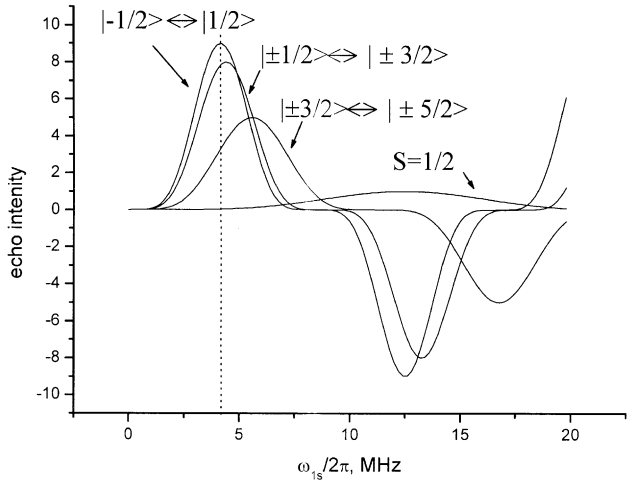

Fig. 2. Plots of the relative factor $K^{M;M-1}_{\mathrm{HYSC};\times}$ of the HYSCORE experiment (not including $\Delta\rho_{M;M-1}$), Eq. (19), for the various EPR transitions in a $S = 5/2$ system and of a $S = 1/2$ system as a function of the MW field $\omega_{1S}/2\pi$, for pulse lengths of 20 ns for p_1, p_2, and p_3 and 40 ns for p_4. The dashed line marks the value of $\omega_{1S}/2\pi$ for which a maximum echo intensity for the $|-1/2\rangle - |1/2\rangle$ transition is obtained.

account, the EPR spectrum should be simulated including the ZFS term and the specific orientations that contribute to the echo at a given field and irradiation settings should then be determined. Fig. 3 shows an example of the experimental two-pulse field-sweep echo-detected (FS-ED) EPR spectrum of $Mn(D_2O)^{2+}_6$ and simulations obtained with spin Hamiltonian parameters

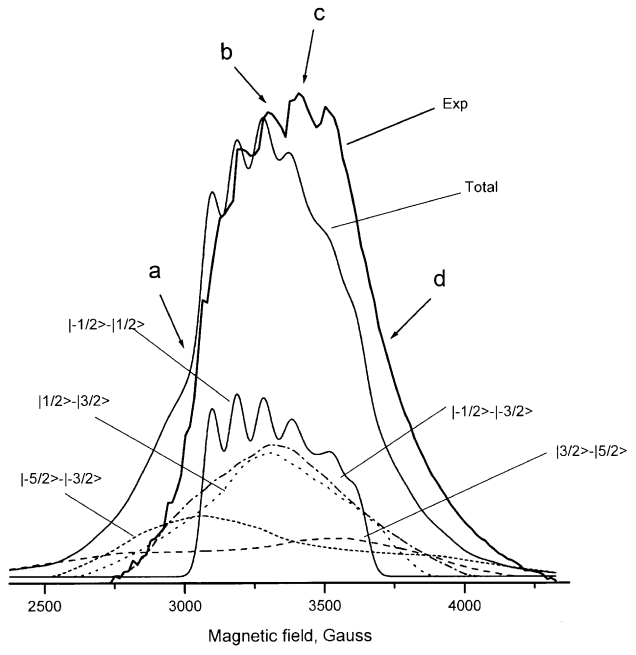

Fig. 3. Simulated X-band EPR powder patterns of the various transitions in Mn^{2+} and the total spectrum obtained with $D = -555$ MHz, $E/D = 0.1$, $a_{\mathrm{iso}}(^{55}\mathrm{Mn}) = 225$ MHz and $T = 8$ K (line width for the $|-1/2\rangle \leftrightarrow |1/2\rangle$ transition was 140 MHz and for all others 196 MHz), compared with the experimental FS-ED EPR spectrum of $Mn(D_2O)^{2+}_6$ reworded at 8 K with $\tau = 0.35\,\mu$s.

taken from Ref. [25], and taking into account the nutation and population factors optimized for the $|-1/2\rangle \leftrightarrow |1/2\rangle$ transition (see Table 1). The nuclear modulation effect was not included and we believe that it is the major reason for the deviations between the experimental and calculated traces [26,27].

3. Experimental

Samples of 2 mM $VO(D_2O)^{2+}_5$ and $Mn(D_2O)^{2+}_6$ were prepared by dissolving the appropriate amounts of $MnCl_2$ and $VOSO_4$ in 50:50 water:glycerol. Pulsed EPR experiments were carried out at ~ 8.5 GHz and 8 K, using a homebuilt spectrometer [28]. FS-ED EPR spectra were recorded using the two-pulse echo sequence with MW pulses of 20 and 40 ns, respectively. The HYSCORE spectra were recorded using the sequence shown in Fig. 1a [4], where the echo is measured as a function of t_1 and t_2. The duration of both the $\pi/2$ and π pulses was 30 ns, while the amplitude of the π pulse was twice that of the $\pi/2$ pulses. The increment of t_1 and t_2 was 40 ns and (130×130) points were collected. The appropriate phase cycles, eliminating unwanted echoes, were employed in all experiments [23].

The HYSCORE data were treated with the Bruker WINEPR software. The background decay in both the t_1 and t_2 dimensions was removed using a polynomial fit, the data were then apodized with Hamming or sinbell windows and after zero filling to 512 points in each dimension, Fourier transformation (FT) was carried out in the two dimensions. The spectra shown are contour plots in magnitude mode with a linear scaling of the contour intervals.

3.1. Simulations

The Mn^{2+} EPR simulations were carried out using a program developed in-house employing third order perturbation theory [29]. The HYSCORE simulations were performed using two simulation programs. The first is a modified version of TRYSCORE [8] where the representation of the Hamiltonian in terms of a two block diagonal form corresponding to the nuclear Hamiltonian H_α and H_β has been changed to that corresponding to a specific EPR transition, H^I_M, H^I_{M-1} (Eq. (2)) as described in the previous sections. The ZFS was not taken into account in the ESEEM calculations, except in some cases where it was used in the calculation of relative intensity factors (based on simulations of the EPR spectra) of the various transitions to generate a total HYSCORE spectrum. In this program, the H^I_M matrices were diagonalized numerically and therefore they were not limited to small quadrupole couplings, as opposed to the description given in the present work. The second program used was "autodiaGal" which is

based on the approach presented in this work. All the simulated 1D ESEEM spectra and some HYSCORE spectra were obtained using the second program. Both programs gave the same results for the Hamiltonian parameters used in this work (small nqi).

4. Results

4.1. Simulations

4.1.1. Two-pulse ESEEM spectra

Fig. 4 shows the sum and the individual contributions of the various EPR transitions of an $S = 5/2$ system with an isotropic g-factor and a weakly coupled proton to the two-pulse ESEEM spectrum (amplitude mode). In the sum spectrum- the sub-spectra were weighted only according to the nutations factors, Eqs. (14) and (20), where the pulses were optimized for the central $|-1/2\rangle \leftrightarrow |1/2\rangle$ transition. For this simple system, the orientation-dependent ENDOR/ESEEM frequencies are given by:

$$\nu_{I;M} = [(\nu_{0I} + MA)^2 + M^2B^2]^{1/2}, \tag{23}$$

where $\nu_{0I} = \omega_{0I}/2\pi$. For an axial hfi, $A = a_{\text{iso}} + T_\perp (3\cos^2\vartheta - 1)$ and $B = 3T_\perp \cos\vartheta \sin\vartheta$, where ϑ is the angle between the principal z-axis of the hfi and the magnetic field, a_{iso} is the isotropic hyperfine coupling, and $-T_\perp$ is the perpendicular anisotropic component. The powder pattern of the $|-1/2\rangle \leftrightarrow |1/2\rangle$ transition (Fig. 4) is the narrowest, as expected from Eq. (23), due to the smallest magnitude of the anisotropic contributions, $|MT_\perp|$. A more detailed description of the powder lineshapes is given in Appendix C. In the following, we shall refer to the ESEEM/HYSCORE frequencies in frequency units labeled by $\nu = \omega/2\pi$ and not in angular units ω as in the theoretical part, to be consistent with the experimental results.

The expression for the two-pulse echo (Eq. (13)) shows that sum and difference modulation frequencies are expected. For $S = 1/2$, and at least for $I = 1/2$ and $I = 1$ with a small nqi, as in ^{2}H, the sum-combination harmonic, $\nu_\alpha + \nu_\beta$, gives rise to a relatively narrow peak, even in orientationally disordered samples [30,31]. The presence of this line in the ESEEM spectra turned out to be most useful as its frequency shift, Δ, from $2\nu_{0I}$ provides directly the anisotropic hfi according to [30]:

$$\Delta \cong 9T_\perp^2/16\nu_{0I}. \tag{24}$$

For $S = 5/2$, the orientational averaging of all the sum-combinations of the ENDOR/ESEEM frequencies $(\nu_{I;M} + \nu_{I;M-1})$ for the $(M \leftrightarrow M-1)$ transitions should include probabilities, depending on the irradiation conditions, temperature, and size of the ZFS. However, as shown in Fig. 4, among all EPR transitions only the ESEEM spectrum arising from the $|-1/2\rangle \leftrightarrow |1/2\rangle$ transition exhibit a narrow combination line due to significant cancellation of the anisotropy introduced by the A term (see Eq. (23)). Consequently, this line is superimposed on a broad background due to the other transitions. A similar behavior is expected for the four-pulse experiment.

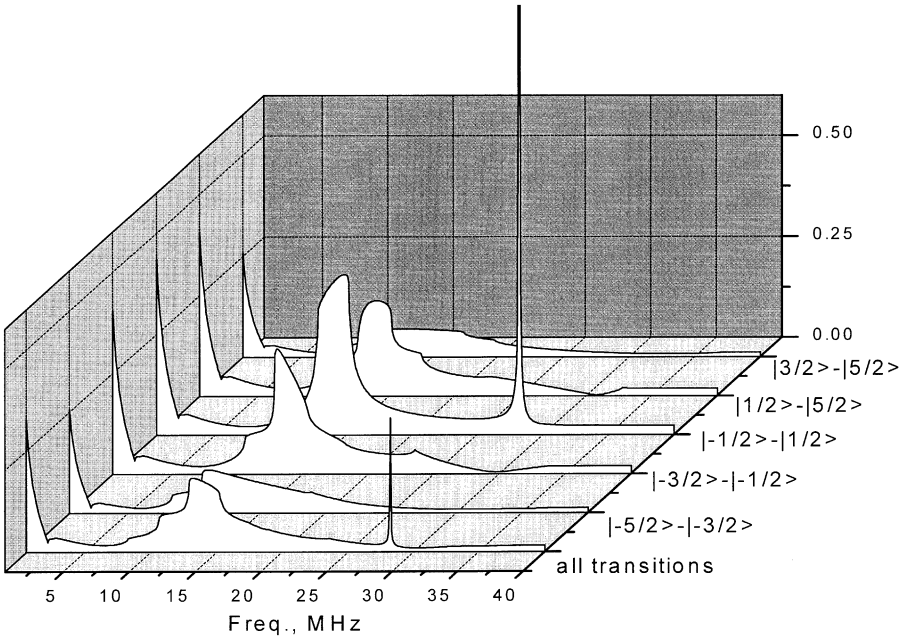

Fig. 4. The individual sub-spectra of two-pulse ESEEM (magnitude mode), along with their sum (weighted according to the relative nutation angles with the central $|1/2\rangle \leftrightarrow |-1/2\rangle$ transition taken as reference) for a single proton coupled to an $S = 5/2$ electron-spin multiplet with $a_{\text{iso}} = -0.6$ MHz $T_\perp = 1.70$ MHz and $B_0 = 3300$ G.

4.1.2. Cross-peak lineshapes in HYSCORE spectra

In this section, we describe the characteristics of the HYSCORE cross-peaks for each of the EPR transitions for $S = 3/2, 5/2$ systems under the conditions of weak to intermediate couplings. We begin with the simplest system, $S = 3/2$ coupled to one nucleus with $I = 1/2$ with hyperfine parameters that are relevant to ^{15}N. We chose ^{15}N rather than ^{1}H because the ^{1}H high Larmor frequency leads to relatively high ESEEM frequencies in the case of transitions other than $|-1/2\rangle \leftrightarrow |1/2\rangle$, which may be difficult to observe experimentally. Fig. 5 shows the HYSCORE spectra, corresponding to each of the EPR transitions. The parameters used are appropriate for a directly coordinated nitrogen of an imidazole ligand (see figure caption for details) and they correspond to a situation between strong and weak coupling. No broadening was added to the spectra to allow a clear observation of the shapes of the ridges. A simple way to understand the cross-peak characteristics in orientationally disordered systems is to consider only the extrema and the singularities of the ENDOR frequencies, as given in Eq. (B.4). The pattern of the $|-1/2\rangle \leftrightarrow |1/2\rangle$ transition is similar to that observed for $S = 1/2$ and the peaks appear in both $(-,+)$ and $(+,+)$ quadrants. To first order, they are centered around ν_{0I} and they run perpendicular to the diagonal (along $\nu_1 = \nu_2$) such that the projection on each of the frequency axes has the same width and give the hyperfine anisotropy (this is more obvious in Fig. 6). In the present case- the first order description fails due to the matching condition $|2a_{\rm iso} + T_\perp| \cong 4\nu_{0I}$, which is approximately satisfied for $M = -1/2$ and the deviation from a 45° slope for the ridges becomes large.

In the other EPR transitions, the identical sign of M and $M - 1$ leads to ridges that run along the diagonal, but not parallel to it, since the effective anisotropy is different in the $M = \pm 1/2$ and $M = \pm 3/2$ manifolds. The line that goes through the centers of the ridges for the transition $|1/2\rangle \leftrightarrow |3/2\rangle$ (marked as a dotted line on the spectrum in Fig. 5) intercepts the diagonal at a point corresponding to $\nu_{0I} + a_{\rm iso} + T_\perp/2 = 4.05\,\text{MHz}$, while the corresponding point for the $|-3/2\rangle \leftrightarrow |-1/2\rangle$ transition is $|\nu_{0I} - (a_{\rm iso} + T_\perp/2)| = 1.21\,\text{MHz}$. These points should be identical to the midpoints of the skyline projections for the pairs of ridges considered. The above numerical values agree with the general first order expression obtained by the simple arithmetic average $|\langle \nu_M + \nu_{M-1}\rangle| = |\nu_{0I} + (M - 1/2)\cdot(a_{\rm iso} + T_\perp/2)|$ of the center of the cross-peaks of the transition $(M \leftrightarrow M - 1)$, obtained from Eq. (B.4). The peaks of the $|-3/2\rangle \leftrightarrow |-1/2\rangle$ transition appear almost parallel to one of the axes due to the approximate matching condition, which is met for the $M = -1/2$ manifold involved in this transition. A more detailed analysis of the shapes of the ridges using analytical expressions for the $I = 1/2$ case is given in Appendix B. The arguments used above concerning the ridge extension and projections are roughly valid for higher nuclear spins too. The presence of a

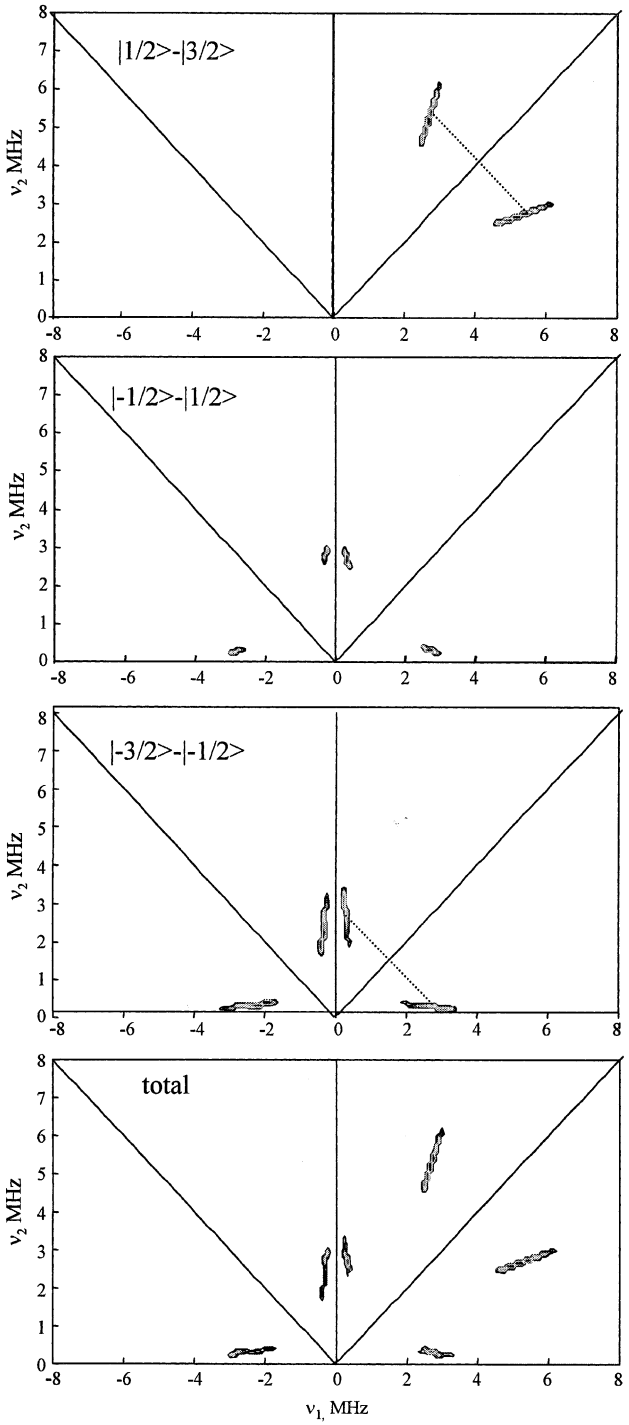

Fig. 5. Simulated HYSCORE spectra of the individual EPR transitions for $S = 3/2$ coupled to an ^{15}N nucleus ($I = 1/2$). Parameters: $a_{\rm iso} = 2.44\,\text{MHz}$; $T_\perp = 0.39\,\text{MHz}$; $\nu_{0I} = 1.42\,\text{MHz}$ (corresponding to static field 3300 G). These parameters are typical for the imidazole nitrogen in high-spin Co^{2+} complexes [38]. In the sum spectrum the sub-spectra were weighted only on the basis of the different nutation frequencies and transition probabilities.

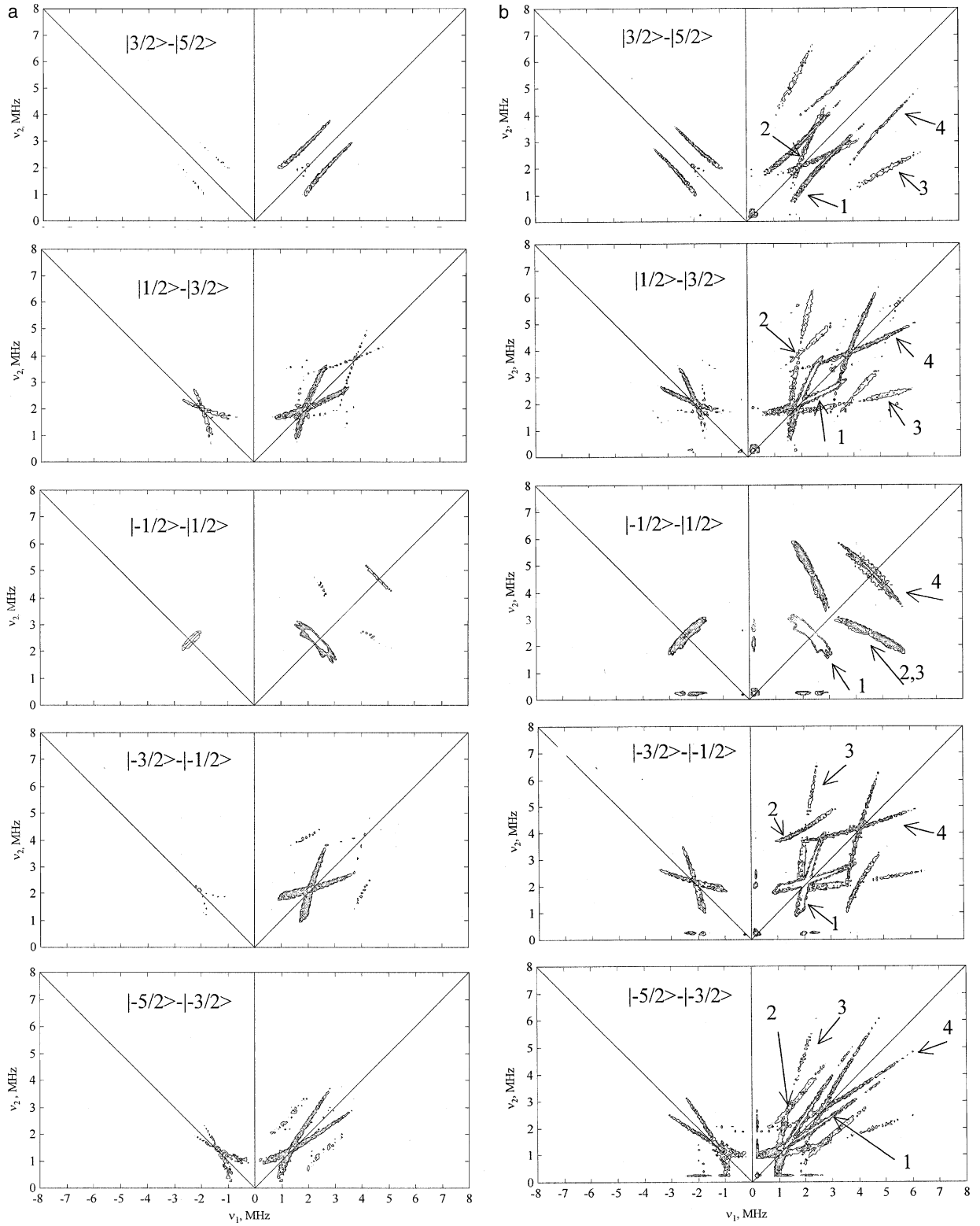

Fig. 6. Simulated HYSCORE spectra of (a) one and (b) two ^{2}H nuclei coupled to an $S = 5/2$ system, showing the sub-spectra corresponding to each of the EPR transitions and (c) their sum, weighted according to the nutation frequencies (optimized for the $|-1/2\rangle \leftrightarrow |1/2\rangle$ transition), temperature, and relative EPR intensity at the field of 3387 G (obtained from simulations of the EPR spectrum). The parameters used in the simulations were: $a_{iso} = 0.1$ MHz, $T_{\perp} = 0.8$ MHz, $e^2qQ/h = 0.2$ MHz, and $\eta = 0.15$ MHz. In all spectra the ridges labeled "1" correspond to ($\nu_M^{sq1,2}$, $\nu_{M-1}^{sq1,2}$), "2" to (ν_M^{dq}, $\nu_{M-1}^{sq1,2}$), "3" to ($\nu_M^{sq1,2}$, ν_{M-1}^{dq}), and "4" to (ν_M^{dq}, ν_{M-1}^{dq}).

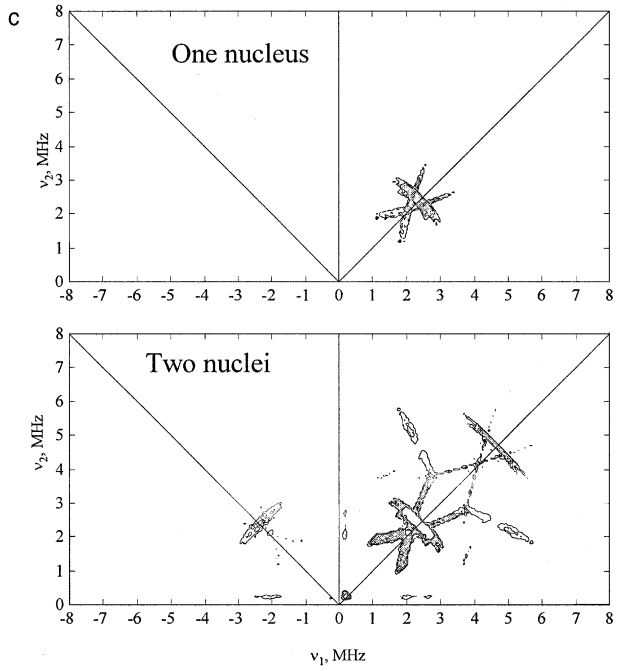

Fig. 6. (*continued*)

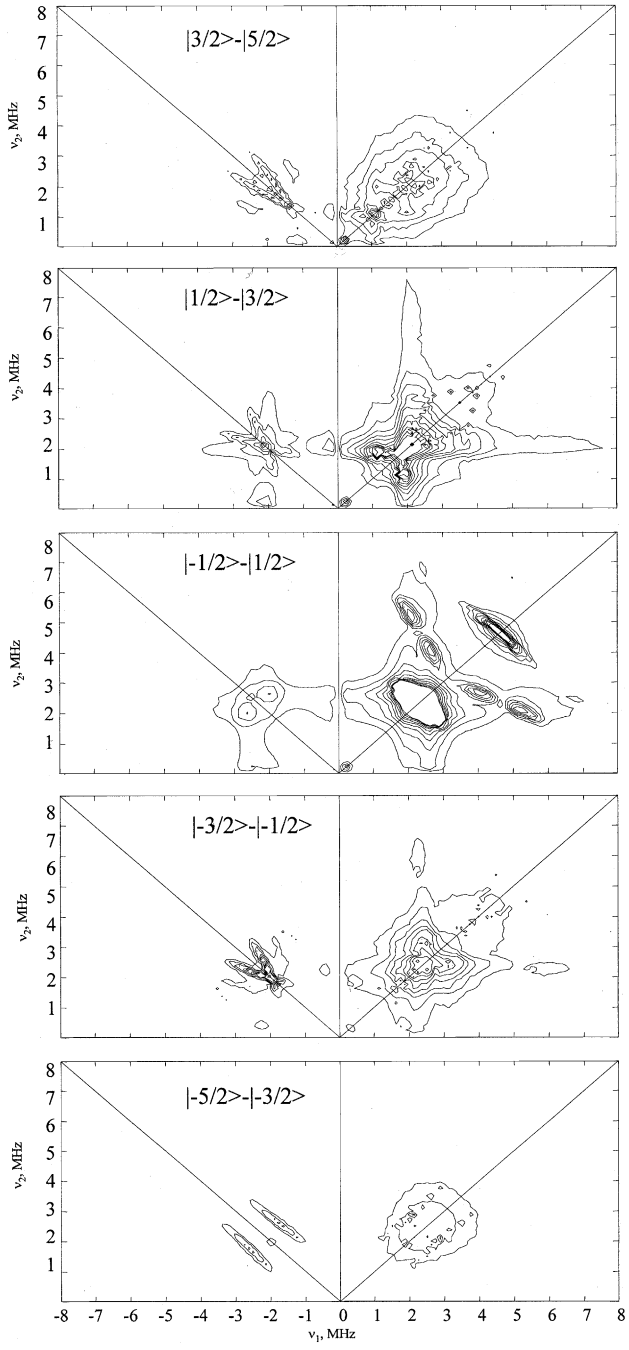

Fig. 7. Similar to Fig. 6b after apodization with a Hamming window.

significant a_{iso} is manifested by a well-noticed shift of the cross-peaks along the diagonal and a better resolution of the contributions of the different manifolds.

Fig. 6 shows the calculated HYSCORE spectra corresponding to each of the EPR transitions for $S = 5/2$ coupled to a single deuterium nucleus, $I = 1$, where a small typical quadrupole interaction ($e^2qQ/h = 0.2$ MHz) appropriate for deuterons [32] has been taken into account. In these simulations, a_{iso} is small and the hfi parameters were taken from those of $Mn(H_2O)_6^{2+}$ [25] scaled according to the appropriate γ ratio. For $I = 1$, there are three nuclear frequencies for each electron-spin manifold, two corresponding to single quantum nuclear transition, labeled ν_M^{sq1} and ν_M^{sq2}, and the third corresponding to a double quantum nuclear transition, labeled ν_M^{dq}. When e^2qQ/h is small relative to $\nu_{eff}(M) = |\nu_{0I} + MA|$, $\nu_M^{sq1} \cong \nu_M^{sq2} \equiv \nu_M^{sq}$ and $\nu_M^{dq} = 2\nu_M^{dq}$. The 2D spectra in the left column of Fig. 6a represent sub-spectra, corresponding to the individual EPR transitions. They show, in addition to the main two $(\nu_M^{sq}, \nu_{M-1}^{sq})$ ridges, similar to those observed in Fig. 5, additional, weaker ridges corresponding to higher order transitions of the type $(\nu_M^{dq}, \nu_{M-1}^{sq})$, $(\nu_M^{sq}, \nu_{M-1}^{dq})$, and $(\nu_M^{dq}, \nu_{M-1}^{dq})$ as identified in the figure. The intensity of these ridges increases with increasing e^2qQ/h. Since all cross-peak pairs are symmetric with respect to the diagonal, for the sake of brevity in the following we shall refer only to one of them. In the absence of a line width, contour plots do not portray well the relative intensities. For example, the intensities of the ridges in the $(+,+)$ quadrant of the $|3/2\rangle \leftrightarrow |5/2\rangle$ transition are rather low as clearly shown in Fig. 7 where a line width has been introduced.

The spectra shown in Fig. 6b were calculated with the same parameters but with two identical nuclei. The main difference between the two sets is the increased intensity of the high order peaks for the two-nuclei case. This is expected considering the relation used to calculate the HYSCORE echo intensity for n nuclei [31]:

$$\langle S_+(\tau;t_1,t_2)\rangle^{M;M-1,\mathrm{tot}}_{\mathrm{HYSC},x} \equiv F\left[\prod_{I=1}^{n}\frac{1}{2I+1}V^I_{M;M-1,x}(\tau;t_1,t_2) + \prod_{I=1}^{n}\frac{1}{2I+1}V^I_{M-1,M,x}(\tau;t_1,t_2)\right], \tag{25}$$

where $V^I_{M;M-1}(\tau;t_1,t_2)$ and $V^I_{M-1;M}(\tau;t_1,t_2)$ are given in Eq. (18) and F is a multiplication factor in analogy to the $S=1/2$ case. Eq. (25) shows that combination frequencies within each manifold are generated. Fig. 6c presents the superposition of the sub-spectra, weighted according to the nutation frequencies, temperature of 8 K, and relative intensities of the EPR transitions at 3387 G (see Fig. 3). This shows that the contributions from all transitions other than the $|-1/2\rangle \leftrightarrow |1/2\rangle$ transition are reduced due to extensive inhomogeneous broadening in orientationally disordered systems. The total spectrum also shows that a significant decrease in resolution is expected when all transitions contribute to the echo.

To allow a clear observation of the shapes of the ridges of various EPR transitions, all spectra shown in Fig. 6 were displayed without the introduction of a line width that accounts for the echo decay and nuclear spin relaxation. Such a situation is, unfortunately, never encountered experimentally and Fig. 7 shows the sub-spectra of the two-nuclei case after apodization with a Hamming window similar to that used experimentally. These spectra show that the contributions of all the transitions, except $|-1/2\rangle \leftrightarrow |1/2\rangle$, appear primarily as extension along the diagonal, with a general loss of resolution. Comparison of the spectra of one and two nuclei (Figs. 6 and 7) shows that the appearance of high order peaks is primarily a consequence of the presence of several nuclei and originate from the $|-1/2\rangle \leftrightarrow |1/2\rangle$ transition and not from the high-spin character of the system. The contribution of the other transitions to the high order peaks is just too weak, at least for the present set of parameters.

4.2. Experimental spectra

The HYSCORE spectra of $VO(D_2O)_5^{2+}(S=1/2)$ and $Mn(D_2O)_6^{2+}(S=5/2)$ in frozen solutions were compared to verify the above lineshape predictions and assess the relative contributions of the various EPR transitions. Fig. 8 displays the FS-ED EPR and two HYSCORE spectra of $VO(D_2O)_5^{2+}$ recorded at field position (a), where all orientations contribute to the echo, and at position (b), where only complexes which have their $g_\perp$ direction parallel to the magnetic field are selected. In addition to the peaks corresponding to $(\nu^{sq}_{1/2}, \nu^{sq}_{-1/2})$, centered at (2.5, 2.5) MHz, cross-peaks of the type $(\nu^{sq}_{1/2}, \nu^{dq}_{-1/2})$ and $(\nu^{dq}_{1/2}, \nu^{dq}_{-1/2})$ at (2.5, 4.5–7) MHz

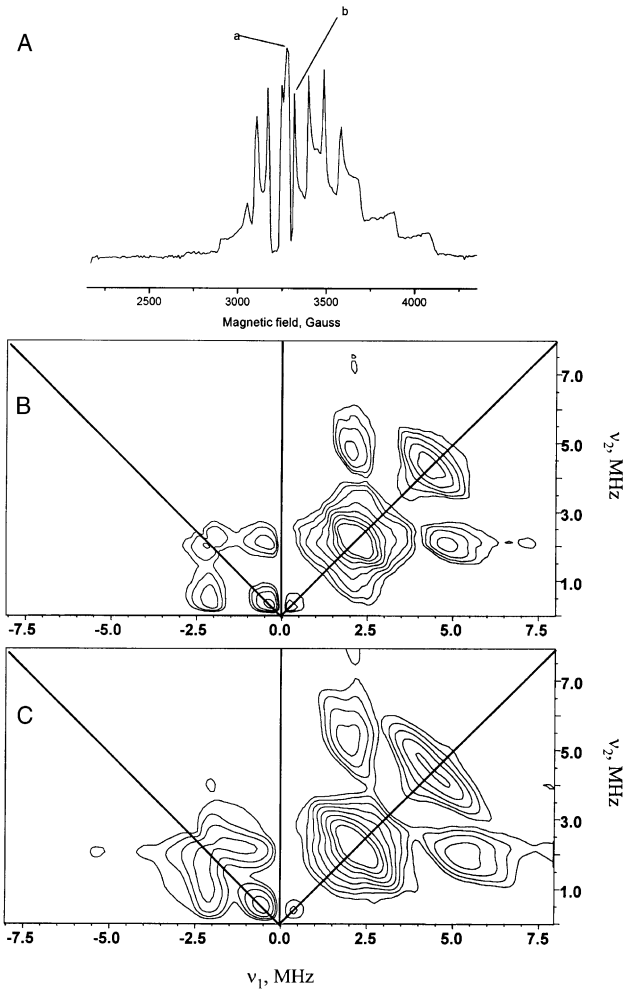

Fig. 8. (A) ED-EPR spectrum of $VO(D_2O)_5^{2+}$ and experimental HYSCORE spectra of $VO(D_2O)_5^{2+}$ recorded at 3274 (B) and 3308 (C). These fields correspond to positions a and b, respectively, in the echo-detected EPR spectrum. The spectra were recorded at 8 K and with pulse delay $\tau = 0.33\,\mu s$.

and (4.8, 4.8) MHz, respectively, appear. These are due to the presence of a large number (10) of deuterons (see Eq. (25)).

Spectra of $Mn(D_2O)_6^{2+}$ recorded at several B_0 values within the EPR powder pattern are shown in Fig. 9. Two spectra (b, c) were recorded with the magnetic field set within the center of the EPR powder pattern, where the dominating contributions are from the $|-1/2\rangle \leftrightarrow |1/2\rangle$ and $|\pm 3/2\rangle \leftrightarrow |\pm 1/2\rangle$ transitions (see Fig. 3). The spectra are rather similar, the main differences are in the width of the $(\nu^{sq}_{1/2}, \nu^{sq}_{-1/2})$ and $(\nu^{dq}_{1/2}, \nu^{dq}_{-1/2})$ peaks along the perpendicular to the diagonal $(\nu_1 = -\nu_2)$. In both spectra, higher order cross-peaks at $(3\nu^{sq}_{1/2}, \nu^{sq}_{-1/2})$, $(3\nu^{sq}_{1/2}, 2\nu^{sq}_{-1/2})$, and $(3\nu^{sq}_{1/2}, 3\nu^{sq}_{-1/2})$ appear. The spectrum recorded at field positions (a), where the relative contribution of the $|-1/2\rangle \leftrightarrow |1/2\rangle$ transition is expected to be significantly diminished, is not very different from the other two, except that the lineshape of

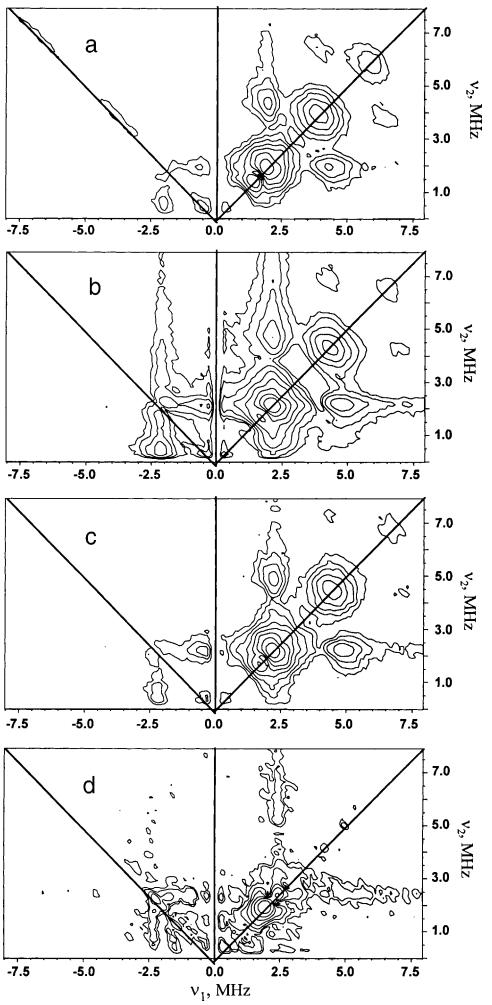

Fig. 9. Experimental HYSCORE spectra of $Mn(D_2O)_6^{2+}$ recorded at (a) 3000, (b) 3276, (c) 3387, and (d) 3670 G. The spectra were recorded at 8 K, $\tau = 0.33\,\mu s$ and MW pulses of 30 ns.

the $(\nu^{sq}_{1/2}, \nu^{sq}_{-1/2})$ peak has changed. It narrowed in the $\nu_1 = -\nu_2$ direction (as compared to the (b) spectrum). The HYSCORE spectrum recorded at 3670 G, where the relative intensity of the $|-1/2\rangle \leftrightarrow |1/2\rangle$ transition should also be significantly reduced, is depicted in Fig. 9d. There, the modulation depth was lower and the peak centered at (2.5, 2.5) MHz became significantly narrower along the $\nu_1 = -\nu_2$ direction. This set of spectra shows that the elongation of the peak, centered at the ^2H Larmor frequency along the diagonal, is induced by the reduction in the relative contributions from the $|-1/2\rangle \leftrightarrow |1/2\rangle$ transition, which usually extends along the $\nu_1 = -\nu_2$ direction, at the expense of the other transitions that run more parallel to the diagonal, as shown in Fig. 6.

Comparison with the spectra of $VO(D_2O)_5^{2+}$ (Fig. 8) shows that the ridges in the $(-,+)$ quadrant do not originate from any of the $M \leftrightarrow M-1$ transitions with $M = \pm 3/2, \pm 5/2$. In addition, the shape of the $(\nu^{dq}_{1/2}, \nu^{dq}_{-1/2})$ and $(2\nu^{sq}_{1/2}, 2\nu^{sq}_{-1/2})$ cross-peaks for Mn(II) is more "square" and less elongated along the $\nu_1 = -\nu_2$ direction, probably due to contributions of the $|\pm 1/2\rangle \leftrightarrow |\pm 3/2\rangle$ and $|\pm 3/2\rangle \leftrightarrow |\pm 5/2\rangle$ transitions and of autocorrelation peaks. The higher intensity of the higher order peaks $[(3\nu^{sq}_{1/2}, 2\nu^{sq}_{-1/2})$ and $(3\nu^{sq}_{1/2}, 3\nu^{sq}_{-1/2})]$ is attributed primarily to the presence of more interacting nuclei (12 vs. 10).

We have tried to isolate the contributions of the $|\pm 3/2\rangle \leftrightarrow |\pm 1/2\rangle$ and $|\pm 5/2\rangle \leftrightarrow |\pm 3/2\rangle$ transitions by recording the spectra with different MW power. According to Fig. 2, the contributions of the $|-1/2\rangle \leftrightarrow |1/2\rangle, |\pm 1/2\rangle \leftrightarrow |\pm 3/2\rangle$ transitions reach maximum at a lower power than the $|\pm 3/2\rangle \leftrightarrow |\pm 5/2\rangle$ transitions. Hence, by increasing the power, the relative intensities of the latter should increase. Fig. 10 presents spectra recorded at a field of 3387 G with fixed pulse length and different power settings. The spectrum shown in Fig. 10a was recorded with an MW power optimized for a maximum echo intensity, whereas that shown in Fig. 10b was recorded with a significantly higher power to augment the contribution of the $|\pm 3/2\rangle \leftrightarrow |\pm 5/2\rangle$ transitions. This led to rather minor changes in the spectrum; narrowing along the $\nu_1 = -\nu_2$ direction, consistent with increased contribution of the $|\pm 3/2\rangle \leftrightarrow |\pm 5/2\rangle$ transitions, and increased intensities of the high order peaks of the type $(3\nu^{sq}_{1/2}, 2\nu^{sq}_{-1/2})$ and $(3\nu^{sq}_{1/2}, 3\nu^{sq}_{-1/2})$.

We have shown through ESEEM simulations that in $S = 5/2$, as in $S = 1/2$ systems, sum combinations

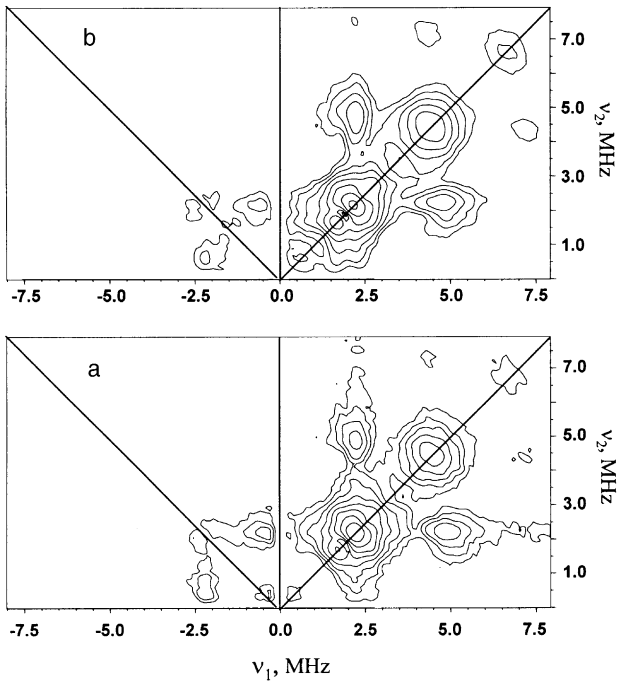

Fig. 10. HYSCORE spectra of $Mn(D_2O)_6^{2+}$ recorded at 3387 G with fixed pulse lengths of 30 ns and different power settings. The spectrum shown in (a) was recorded with optimized power for a maximum total echo intensity (13 dB) whereas that shown in (b) was recorded with significantly higher power (7 dB).

arising from the central transition are expected, although with a relatively lower intensity. Two- and four-pulse ESEEM experiments on $Mn(H_2O)_6^{2+}$ and $Fe(H_2O)_6^{2+}$ have been carried out, and although a strong peak at $2\nu_{0I}$ of the protons was observed, a shifted peak similar to that observed for $Cu(H_2O)_6^{2+}$ [33] or $VO(H_2O)_5^{2+}$ [31] has not been detected. Similarly, Mims et al. [14] have observed a lower intensity for the $2\nu_I$ features in the two-pulse waveform of solutions of $FeCl_3$. Currently, we have no explanation for the absence of these lines and we can only speculate that it may be due to some effect of the ZFS that was not taken into account in our simulations.

5. Discussion

The HYSCORE spectra of half-integer high-spin systems, such as the Kramers' multiplets $S = 3/2$ or $S = 5/2$, consist in principle, of inter-M-manifold correlations corresponding to each of the allowed EPR transitions. In orientationally disordered systems these, correlations exhibit lineshapes with characteristics that are strongly dependent on the $M; M-1$ values involved. When $|a_{\rm iso}| > |T_\perp|$ cross-peaks corresponding to the different transitions are well separated and informative. For example, when $T_\perp$ is small with respect to the line width and cannot be evaluated from the $|-1/2\rangle \leftrightarrow |1/2\rangle$ cross-peaks, it may be determined from those of the $|\pm 1/2\rangle \leftrightarrow |\pm 3/2\rangle$ or $|\pm 3/2\rangle \leftrightarrow |\pm 5/2\rangle$ transitions, where the anisotropy increases by a factor of 3 or 5, at least in one dimension. In contrast when $|a_{\rm iso}| < |T_\perp|$, the presence of cross-peaks due to a number of EPR transitions is actually troubling as they all overlap, reduce the resolution, and consequently impede spectral analysis and the extraction of hfi and nqi parameters. This is the situation for $Mn(D_2O)_6^{2+}$, where the spectrum, although dominated by the $|-1/2\rangle \leftrightarrow |1/2\rangle$ transition, is less resolved and has more signals on the diagonal compared to the corresponding $S = 1/2$ system.

Another complication is the assessment and control of the contribution of the various transitions to the HYSCORE spectrum. One of the experimental parameters capable, in principle, to control this is the strength of the MW irradiation field due to the different nutation frequencies of the various EPR transitions. Unfortunately, those of the $|-1/2\rangle \leftrightarrow |1/2\rangle$ and $|\pm 1/2\rangle \leftrightarrow |\pm 3/2\rangle$ have a rather similar behavior and therefore one should concentrate on the $|\pm 3/2\rangle \leftrightarrow |\pm 5/2\rangle$ transitions. These, however, have the largest inhomogeneous broadening due to the ZFS and therefore their relative contribution to the signal is low and, consequently, the experimental implementation of this approach has failed. Another possibility is to select different transitions by choosing the appropriate magnetic field at which the HYSCORE spectrum is measured. This approach works well when the ZFS is relatively small such that the $|-1/2\rangle \leftrightarrow |1/2\rangle$ signals are very narrow, as observed for Mn(II) complexes at high fields [34,35]. But, at X-band the central transition is often too broad and this requires measurements at the extreme edges of the spectrum where the signal becomes again too weak. Hence, it is expected that for most practical cases it is the $|-1/2\rangle \leftrightarrow |1/2\rangle$ transition that will dominate the spectrum.

In light of the above, to profit from the unique features of the various cross-peaks of the $|\pm 1/2\rangle \leftrightarrow |\pm 3/2\rangle$ and $|\pm 3/2\rangle \leftrightarrow |\pm 5/2\rangle$ transitions, other methods to resolve them have to be devised. It is possible that an approach similar to that suggested by Hofbauer and Bittl [36] where the time window at which the echo is sampled is varied may yield the desired resolution.

6. Summary and conclusions

General expressions for the echo intensity in several ESEEM and HYSCORE experiments for $S > 1/2$ systems and a small ZFS were derived. The characteristics of the HYSCORE cross-peaks arising from the different EPR transitions, under conditions of selective excitation, were explored using simulations, specifically for half-integer spins, $S = 3/2, 5/2$. It was found that under conditions of weak hyperfine couplings and a dominating anisotropic hyperfine interaction, the peaks of the various EPR transitions overlap and thus reduce the resolution of the spectrum. In contrast, when the isotropic hyperfine is larger than the anisotropic part, the individual contributions of all transitions are resolved and can be used to extract the anisotropic part more accurately. Experimental HYSCORE spectra of $Mn(D_2O)_6^{2+}$ in a frozen solution showed a behavior of a larger anisotropic hyperfine interaction and the spectrum is dominated by the $|-1/2\rangle \leftrightarrow |1/2\rangle$ transition. The effect of the other transitions is limited to the increased intensity of signals on the diagonal and a reduction in the spectral resolution.

In addition, some useful and simple analytical derivations available for the $S = 1/2$, $I = 1/2$ case were extended for $S > 1/2$: (i) An analytical expression for the generalized modulation depth was given. It predicts that an enhanced intensity of nuclear modulations should arise from forbidden EPR transitions for which $|\Delta M| = 2$. (ii) The components of an axially symmetric hfi were related to "geometrical" parameters derived from the shapes of the HYSCORE cross-peaks of each of the EPR transitions. (iii) An analytical expression for the powder ENDOR lineshapes for an axially symmetric hfi was derived. This is useful to predict the basic characteristics of the ESEEM and HYSCORE.

Acknowledgments

This work was supported by a grant from the Israeli Science Foundation. N.P.B. wants to thank the team of the Chemical Physics Department in Rehovot for their hospitality and Professor Anders Lund and Einar Sagstuen for their encouragement. We thank Dr. Patrick J. Carl for his help in the modification of the TRYSCORE program.

Note added in proof

In a recent publication (A.V. Astashkin and A.M. Raitsimring *J. Chem. Phys.*, 117, 2002) it was shown that the ZFS introduces inhomogeneous broadening to the sum combination peaks of the $|-1/2\rangle - |1/2\rangle$ transition which accounts for its low intensity.

Appendices: Analytical expressions for axial $S = 5/2$, $I = 1/2$ system

Appendix A. Modulation-depth factor

For a nucleus with $I = 1/2$ and an axially symmetric hfi interaction, an explicit expression for the modulation depth, $k_{M;M'}$, similar to that existing for $S = 1/2$ system [2,3,18], can be derived, yielding:

$$k_{M;M'} = \sin^2 \vartheta_t^{M;M'} = \frac{B^2 v_{0I}^2}{v_{I;M}^2 v_{I;M'}^2 + B^2 v_{0I}^2 (1 - |\Delta M|^2)}, \quad \text{(A.1)}$$

where $|\Delta M| = |M - M'|$. Since usually $\Delta M = 1$ the second term in the denominator vanishes and Eq. (2) reduces to that given in reference [2] for $S > 1/2$. The ENDOR/ESEEM frequencies, $v_{I;M}$ for axial systems are given in Eq. (23) or Eq. (C.2). The relation in Eq. (A.1) reduces to the usual modulation depth factor $k_{\alpha;\beta}$ for $S = 1/2$ [2,3].

The appearance of $|\Delta M|$ in the denominator of Eq. (A.1) shows that if a forbidden EPR transition, such as a electronic double quantum transition with $|\Delta M| = 2$, can be excited, the nuclear modulation effect can be enhanced. This effect can be important for nuclei with low modulation depth for $|\Delta M| = 1$. However, since the excitation of forbidden EPR transitions with $|\Delta M| = 2$ become possible when the ZFS is non-negligible, the relation given in Eq. (A.1) should be reevaluated under conditions of finite ZFS. Nonetheless, we assess that its essence will most probably not change significantly.

Appendix B. Cross-peaks and hyperfine parameters in HYSCORE powders

Following the derivation of Dikanov et al. [6,7] which describes the cross-peak lineshape for $S = 1/2$, it is possible to derive a similar relation for the ENDOR frequencies, $v_{I;M}$, of an $S = 3/2$ or an $S = 5/2$ system according to:

$$v_{I;M} = F(v_{I;M'}) \equiv \sqrt{Q_{M;M'} v_{I;M'}^2 + G_{M;M'}}. \quad \text{(B.1)}$$

The constants $Q_{M;M'}$ and $G_{M;M'}$ are the slope and the intercept, respectively, of the linear plots of $v_{I;M}^2$ vs. $v_{I;M'}^2$ derived from the cross-peak lineshapes (M and M' define the EPR transition). This type of relation is strictly valid for nuclei with spin $I = 1/2$ with an axially symmetric hfi. It is also accurate for the degenerate transitions of higher half-integer nuclear spins with a negligible nqi.

The slope, $Q_{M;M'}$, can be rewritten in terms of the nuclear Zeeman and the hfi parameters as:

$$Q_{M;M'} = \frac{M[2v_{0I} + M(2a_{\text{iso}} + T_\perp)]}{M'[2v_{0I} + M'(2a_{\text{iso}} + T_\perp)]}. \quad \text{(B.2)}$$

In the limit of a weak hyperfine interaction with respect to v_{0I}, defined by $|2a_{\text{iso}} + T_\perp| \ll 4v_{0I}$, the slope $Q_{1/2;-1/2}$ becomes approximately -1 and the curve $v_{I;1/2} = F(v_{I;-1/2})$ in Eq. (B.1) close to perpendicular to the diagonals. In contrast, for all the other values of M, the projections of the connected pairs have the same sign rendering the slope always positive. For $S = 5/2$, increasing $|M|$ to the maximum value of 5/2 turns the slope closer to unity, generating ridges more parallel to the diagonal.

The expression for the intercept $G_{M;M'}$ is more complicated and will be first given in its most simple form using the $v_\parallel$ and $v_\perp$ singularities of the ENDOR powder patterns.

$$G_{M;M'} = \frac{v_{\parallel M'}^2 v_{\perp M}^2 - v_{\perp M'}^2 v_{\parallel M}^2}{v_{\parallel M'}^2 - v_{\perp M'}^2}, \quad \text{(B.3)}$$

where

$$\begin{aligned} &v_{M\parallel} = v_{0I} + MA_\parallel \quad \text{and} \quad v_{M\perp} = v_{0I} + MA_\perp, \\ &A_\parallel = a_{\text{iso}} + 2T_\perp, \quad A_\perp = a_{\text{iso}} - T_\perp. \end{aligned} \quad \text{(B.4)}$$

For $M' = M - 1$, $G_{M;M'}$ becomes:

$$G_{M;M-1} = \frac{-v_{0I}\left[2v_{0I}^2 + (2M-1)A_\parallel v_{0I} + 2M(M-1)A_\perp A_\parallel\right]}{(M-1)\left[2v_{0I} + (M-1)A_\parallel\right]}. \quad \text{(B.5)}$$

Finally, the hyperfine components can be directly extracted according to:

$$a_{\text{iso}} = \frac{[Q - M(1-Q)]v_{0I} \mp \frac{1}{3}\sqrt{G[M^2 - (M-1)^2 Q] + Qv_{0I}^2}}{M^2(Q-1) - Q(2M-1)}, \quad \text{(B.6)}$$

$$T_\perp = \pm \frac{\sqrt{G[M^2 - (M-1)^2 Q] + Qv_{0I}^2}}{3[M^2(Q-1) - Q(2M-1)]}, \quad \text{(B.7)}$$

where the subscripts $M; M-1$ of $Q_{M;M-1}$ and $G_{M;M-1}$ were omitted for the sake of clarity. Only the upper or the lower sign combinations in both equations can be

combined, thus, generating two different sets of hyperfine parameters. This ambiguity arises from the squared ENDOR frequencies in Eq. (B.1) and the always-positive frequencies in experimental ENDOR and ESEEM spectra. An additional ambiguity originates from the inability to distinguish between the M and M' manifolds. This yields an additional set of similar equations by exchanging M and M' in Eq. (B.1). Alternatively, the above equations can be used twice treating each pair of the symmetric HYSCORE cross-peaks across the diagonal separately. Thus at the most, a total of four different acceptable sets of $a_{\rm iso}$ and $T_\perp$ for each symmetric pair of lines is obtained.

Two additional factors complicate the task of determination of the hyperfine parameters: (i) The presence of an hfi with a rhombic symmetry and a nqi which were not taken into account. (ii) Overlap of the signals from the different EPR transitions as shown in the experimental and simulated spectra presented earlier. There is, however, a good prospect to succeed with the determination of the hyperfine couplings parameters given by Eqs. (B.6) and (B.7) if several transitions $M \leftrightarrow M-1$ can be resolved, assigned, and evaluated for the same system. In that case, the equation system is overdetermined and this property can be used to eliminate some of the four potential solutions.

It has been shown that for $S = 1/2$ $\nu_\parallel$ and $\nu_\perp$ can be determined from the intersection of the cross-peak ridges with the curve $\nu_\alpha + \nu_\beta = 2\nu_{0I}$ [2]. For $S = 5/2$, this holds only for the ridges of the $|-1/2\rangle \leftrightarrow |1/2\rangle$ transition. For the other transitions, the curve to be considered is $\nu_M + \nu_{M-1} = 2\nu_{0I} - A(2M-1)$. The latter depends on A which is orientation dependent and therefore not very useful for determining $\nu_{M\parallel}$ and $\nu_{M\perp}$.

Appendix C. Powder patterns of ENDOR lines

Simulations of the ENDOR powder patterns are often relevant as a reference when the exact expressions of the ESEEM and HYSCORE signals and their lineshape properties are considered in some limiting approximate cases. The quantities $k_{M;M'}$, and the ENDOR/ESEEM frequencies, as well as their linear combinations $\nu_{I;M} \pm \nu_{I;M-1}$, are strongly orientation dependent. Consequently, the numerical superposition over all possible orientations for orientationally disordered samples may exhibit slow convergence, particularly for the highest values of $|M|$ because of its larger effective anisotropy $|\nu_{M\parallel} - \nu_{M\perp}|$. While for the ESEEM experiment this averaging has to be performed numerically due to the complicated orientation dependence of the modulation amplitudes, it was possible to obtain a relatively simple, analytical expression for ENDOR powder lineshape. This is given (to an arbitrary overall factor, the same for all M) by:

$$P_M(\nu) = \frac{\nu}{\sqrt{(\nu_{M\parallel}^2 - \nu_{M\perp}^2)(\nu^2 - \nu_{M\perp}^2)}}, \tag{C.1}$$

where two frequency regions for ν, $\nu_{M\perp} < \nu \leqslant \nu_{M\parallel}$ or $\nu_{M\parallel} < \nu \leqslant \nu_{M\perp}$, are possible for the explicit lineshape functions $P_M(\nu)$, depending on the magnitudes and the signs of the parameters $\nu_{0I}, a_{\rm iso}$, and $T_\perp$ ($\nu_{M\perp}$ and $\nu_{M\parallel}$ are defined in Eq. (B.4)).

In analogy to the expression for the ENDOR frequencies for $S = 1/2$ and an arbitrary orientation given by Dikanov and Bowman [7], we can write:

$$\nu_{I;M}(\vartheta) = [\nu_{M\perp}^2 + (\nu_{M\parallel}^2 - \nu_{M\perp}^2)\cos^2\vartheta]^{1/2}. \tag{C.2}$$

The orientation dependence of the frequency $\nu_{I;M}$, given by Eq. (C.2), is very similar to that of the spherical harmonic $Y_{20}(\vartheta) \propto 3\cos^2\vartheta - 1$, involved in the secular part of the usual magnetic interactions expressed as second order tensors. Thus, similar to the expression derived for powder lineshapes of the g, hfi and nqi

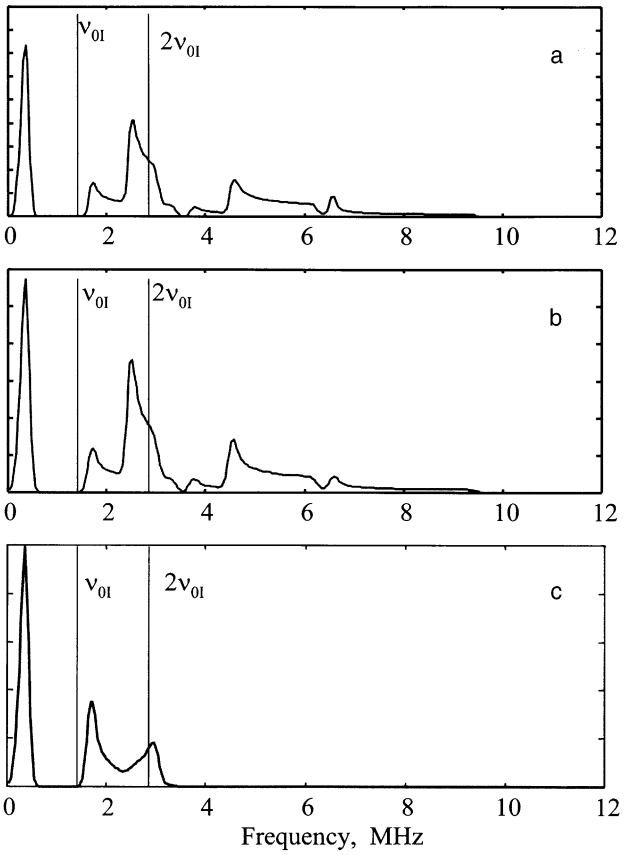

Fig. 11. ENDOR spectra of an ^{15}N nucleus coupled to an $S = 5/2$ system in an orientationally disordered system obtained by (a) numerical averaging and (b) using Eq. (C.3). (c) ESEEM powder pattern obtained by numerical superposition of the ESEEM amplitudes (Eq. (A.1)) on the ENDOR powder. In these computations an equal weight was considered during superposition of the different electronic-transition signals. The parameters used in the simulations were $a_{\rm iso} = 2.44$, $T_\perp = 0.39$; and $\nu_{0I} = 1.42$ MHz, ($B_0 = 3300$ G) [38]. The spectra were convoluted with a Gaussian width a half-height of 0.16 MHz/point.

tensor [39] and using Eqs. (B.4) and (C.2), Eq. (C.1) was derived. Ideally, if all the EPR transition, were uniformly excited (at different orientation subspaces), the relation that follows should be taken as a simplified ENDOR lineshape:

$$P(\nu) = \sum_{M=-S+1}^{S} [S(S+1) - M(M-1)] \cdot [P_M(\nu) + P_{M-1}(\nu)]. \tag{C.3}$$

Otherwise an additional weighing factor should be added. Notice that the first factor under the square root in the denominator of Eq. (C.1) for the lineshape P_M contributes to the variation of the weights of each term in the above sum along with the coefficients $[S(S+1)-M(M-1)]$ in the summation. The relation in Eq. (C.3) was compared with the lineshape obtained from numerical spatial averaging [37], and was found to give identical results for all practical purposes as shown in Fig. 11. It also shows the superimposed ESEEM amplitudes of the basic ENDOR frequencies and their combinations in a uniform spatial-orientation distribution for ideal irradiation conditions. In this case, the weight was taken as $P(\vartheta) = [S(S+1) - M(M-1)]\, k_{M;M-1}(\vartheta) \sin\vartheta$, where $k_{M;M-1}(\vartheta)$ is the relevant modulation depth (see Eq. (A.1)). The depth factor $k_{M;M-1}(\vartheta)$, included in the weight, reduces significantly the contributions of all transitions, except the $|-1/2\rangle \leftrightarrow |1/2\rangle$ transition. The ENDOR signals of the $|-3/2\rangle \leftrightarrow |-1/2\rangle$ are also visible, probably due to satisfaction of matching condition [7,37], $|2a + T_\perp| \cong 4\nu_{0I}$ for $M_S = -1/2$.

Unfortunately, it is not possible to obtain the ESEEM powder pattern by merely multiplying $P_M(\nu)$ with $k_{M;M-1}(\vartheta)$ since the explicit dependence of $P(\nu)$ on ϑ has to be taken into account. An attempt to obtain analytic expressions for the ESEEM powders, as in ENDOR, including $k_{M;M-1}(\vartheta)$ in the statistical weight, was found to be too tedious. To the best of our knowledge, there have been so far no other explicit expressions for ESEEM lineshapes in the literature with the direct functional form $P(\nu)$ as in Eq. (C.1).

References

[1] Y. Deligiannakis, M. Louloudi, N. Hadjiliadis, Electron spin echo envelope modulation (ESEEM) spectroscopy as a tool to investigate the coordination environment of metal centers, Coord. Chem. Rev. 204 (2000) 1–112.

[2] A. Schweiger, G. Jeschke, Principles of Pulse Electron Paramagnetic Resonance, Oxford University Press, Oxford, 2001.

[3] S.A. Dikanov, Yu.D. Tsvetkov, Electron Spin Echo Envelope Modulation (ESEEM) Spectroscopy, CRC Press, Boca Raton, FL, 1992.

[4] P. Höfer, A. Grupp, H. Nebenführ, M. Mehring, Hyperfine sublevel correlation HYSCORE spectroscopy: a 2D ESR investigation of the squaric acid radical, Chem. Phys. Lett. 132 (1986) 279–282.

[5] E.J. Reijerse, J.J. Shane, E. de Boer, P. Höfer, D. Collison, One and two dimensional ESEEM of nitrogen coordinated oxovanadium(iv) complexes, in: N.D. Yordanov (Ed.), Electron Magnetic Resonance of Disordered Systems II, World Scientific, Singapore, 1991;
J.J. Shane, Ph.D. Thesis, University of Nijmegen, 1993, p. 253.

[6] S.A. Dikanov, M.K. Bowman, Determination of ligand conformation in reduced [2Fe–2S] ferredoxin from cysteine β-proton hyperfine couplings, J. Biol. Inorg. Chem. 3 (1998) 18–29.

[7] S.A. Dikanov, M.K. Bowman, Cross-peak lineshape of two-dimensional ESEEM spectra in disordered $S = 1/2$, $I = 1/2$ spin systems, J. Magn. Res. A 116 (1995) 125–128.

[8] R. Szosenfogel, D. Goldfarb, Simulations of HYSCORE spectra obtained with ideal and nonideal pulses, Mol. Phys. 95 (1998) 1295–1308.

[9] W.B. Mims, Envelope modulation in spin-echo experiments, Phys. Rev. B 5 (1972) 2409–2419;
W.B. Mims, Amplitudes of superhyperfine frequencies in electron-spin-echo envelope, Phys. Rev. B 6 (1973) 3543–3545.

[10] B.M. Hoffmann, E. Sturgeon, P.E. Doan, V.J. DeRose, K.E. Lieu, S.J. Lippard, ESEEM and ENDOR magnetic-resonance studies of the non-kramer doublet in the integer-spin Diiron(II) forms of 2-methane monooxygenase hydroxylases and hemerythrin azide, J. Am. Chem. Soc. 116 (1994) 6023–6024.

[11] C.G. Hoogstraten, C.V. Grant, T.E. Horon, V.J. DeRose, R.D. Britt, Structural analysis of metal ion ligation to nucleotides and nucleic acids using pulsed EPR spectroscopy, J. Am. Chem Soc. 124 (2002) 834–842.

[12] B. Schneider, C. Sigalat, T. Amano, J.L. Zimmermann, Evidence for changes in the nucleotide conformation in the active site of H^+-ATPase as determined by pulsed EPR spectroscopy, Biochemistry 39 (2000) 15500–15512.

[13] D.Y. Zhao, Z.H. Luan, L. Kevan, Electron spin resonance and electron spin echo modulation spectroscopy of aluminophosphate-based mesoporous molecular sieve containing framework manganese, J. Phys. Chem. 101 (1997) 6943–6948.

[14] W.B. Mims, J. Peisach, J.L. Davies, Nuclear modulation of the electron spin echo envelope in glassy materials, J. Chem. Phys. 66 (1977) 5536–5550.

[15] A.R. Coffino, J. Peisach, Nuclear modulation effects in high-spin electron systems with small zero-field splittings, J. Chem. Phys. 97 (1992) 3072–3091.

[16] R.G. Larsen, C.J. Halkides, D.J. Singel, A geometric representation of nuclear modulation effects: the effects of high electron spin multiplicity on the electron spin echo envelope modulation spectra of Mn^{2+} complexes of N-ras p21, J. Chem. Phys. 98 (1993) 6704–6721.

[17] R. Vardi, M. Bernardo, H. Thomann, K.G. Strohmaier, D.E.W. Vaughan, D. Goldfarb, X-band pulsed ENDOR study of Fe-57-substituted sodalite — the effect of the zero-field splitting, J. Magn. Reson. 126 (1997) 229–241.

[18] N.P. Benetis, A.R. Sørnes, Automatic spin-Hamiltonian diagonalization for electronic doublet coupled to arbitrary nuclear spins and full anisotropy. Test in theoretical 1-dimensional and 2-dimensional electron-spin echo simulations of model systems, Concepts Magn. Reson. 12 (2000) 410–433.

[19] K-Å. Thuomas, A. Lund, Analysis of EPR with large quadrupole interaction, J. Magn. Reson. 22 (1976) 315–325;
K-Å. Thuomas, A. Lund, Evaluation of hyperfine and quadrupole tensors from ENDOR measurements on single crystals, J. Magn. Reson. 18 (1975) 12–21.

[20] M. Iwasaki, Second-order perturbation treatment of the general spin Hamiltonian in an arbitrary coordinate system, J. Magn. Reson. 16 (1974) 417–423.

[21] A. Abragam, The Principles of Nuclear Magnetism, Clarendon Press, Oxford, 1961.
[22] D. Goldfarb, J.-M. Fauth, Y. Tor, A. Shanzer, Study of Cu(II) binding to chiral tripodal ligands by electron spin echo spectroscopy, J. Am. Chem. Soc. 113 (1991) 1941–1948.
[23] C. Gemperle, G. Aebli, A. Schweiger, R.R. Ernst, Phase cycling in pulse EPR, J. Magn. Reson. 88 (1990) 241–256.
[24] G.H. Reed, G.D. Markham, in: L.J. Berliner, J. Reuben (Eds.), Biological Magnetic Resonance, vol. 6, Plenum Press, New York, 1984, p. 73.
[25] X. Tan, M. Bernardo, H. Thomann, C.P. Scholes, Pulsed and continuous wave electron nuclear double resonance patterns of aquo protons coordinated in frozen solution to high spin Mn^{2+}, J. Chem. Phys. 98 (1993) 5147–5157.
[26] D. Goldfarb, L. Kevan, Effect of nuclear modulation on field-swept electron-spin echo spectra, J. Mag. Reson. 76 (1988) 276–286.
[27] A. Schweiger, R.R. Ernst, Pulsed ESR with longitudinal detection. A novel recording technique, J. Mag. Reson. 77 (1988) 512–523.
[28] J.J. Shane, I. Gromov, S. Vega, D. Goldfarb, A versatile pulsed x-band ENDOR spectrometer, Rev. Sci. Instrum. 69 (1998) 3357–3364.
[29] E. Meirovitch, R. Poupko, Lineshape studies of the electron-spin resonance spectra of manganese protein complexes, J. Phys. Chem. 82 (1978) 1920–1925.
[30] A.V. Astashkin, S.A. Dikanov, Yu.D. Tsvetkov, Spectrometer deadtime: effect on electron spin echo modulation spectra in disordered systems, Chem. Phys. Lett. 136 (1987) 204–208;
S.A. Dikanov, A.V. Astashkin, Yu.D. Tsvetkov, Elimination of the matrix line contribution to electron spin echo modulation, Chem. Phys. Lett. 144 (1988) 251–257.
[31] A.M. Tyryshkin, S.A. Dikanov, D. Goldfarb, Sum combination harmonics in four-pulse ESEEM spectra: study of the ligands geometry in aqua-vanadyl complexes in polycrystalline and glass matrices, J. Magn. Res. Ser. A 105 (1993) 271–283.
[32] A. Weiss, N. Weiden, in: J.A.S. Smith (Ed.), Advances in Nuclear Quadrupole Resonance, vol 4, Heyden, London, 1980, pp. 149–237.
[33] K. Matar, D. Zhao, W. Azelle, W. Daniel, P.G. Harrison, D. Goldfarb, Characterization of Cu(II) sites in Cu/SnO_2 catalysts by electron-spin echo envelope modulation spectroscopy, J. Phys. Chem. 99 (1995) 9966–9973.
[34] B.F. Bellew, C.J. Halkides, J. Gerfen, R.G. Griffin, D.J. Singel, High frequency (139.5 GHz) electron paramagnetic resonance characterization of Mn(II)–$H_2{}^{17}O$ interactions in GDP and GTP forms of p21 ras, Biochemistry 35 (1996) 12186–12193.
[35] P. Manikandan, R. Carmieli, T. Shane, A.J. KalbGilboa, D. Goldfarb, W-Band ENDOR investigation of the manganese-binding site of concanavalin A: determination of proton hyperfine couplings and their signs, J. Am. Chem. Soc. 122 (2000) 3488–3494.
[36] W. Hofbauer, R. Bittl, A novel approach to separating EPR lines arising from species with different transition moments, J. Magn. Reson. 147 (2000) 226–231.
[37] E.J. Reijerse, S.A. Dikanov, Electron-spin echo envelope modulation spectroscopy on disordered systems: lineshape singularities in $S = 1/2$, $I = 1/2$ spin systems, J. Chem. Phys. 95 (1991) 836–845.
[38] S.A. Dikanov, A.P. Spoyalov, J. Hütermann, Exploiting the properties of lineshape singularities in orientationally selected electron-spin echo envelope modulation spectra of $Cu^{2+}(^{15}N\text{-imidazole})_4$ for the determination of hyperfine coupling with the remote imidazole nitrogen, J. Chem. Phys. 100 (1994) 7973–7983.
[39] C.P. Slichter, in: Principles of Magnetic Resonance, third ed., Springer, Berlin, 1990, pp. 605–609.